Key Points:
- Seasonal, MLT, *Kp*, and IMF dependence of VLF auroral hiss are analyzed using 8 years of VLF data from South Pole station
- Occurrence in three MLT sectors (morning, afternoon, and evening) is consistent with the location of *Kp*-dependent auroral boundaries
- Occurrence is more likely under IMF conditions that bring the peak in the upward current system closer to the latitude of the station

Correspondence to:
M. Spasojevic,
mariaspasojevic@stanford.edu

Statistics of auroral hiss and relationship to auroral boundaries and upward current regions

M. Spasojevic[1]

[1]Department of Electrical Engineering, Stanford University, Stanford, California, USA

Abstract An 8 year database of VLF auroral hiss observations from South Pole station (invariant latitude of $-74°$ with magnetic local time (MLT) = UT -3.5 h) is analyzed. There are three peaks in hiss occurrence as a function of MLT in the evening sector (19–23 MLT), afternoon sector (13–17 MLT), and morning sector (7–11 MLT). The geomagnetic and interplanetary magnetic field (IMF) drivers of hiss are examined in the three MLT sectors, and the results are interpreted using an empirical model of auroral boundaries and an empirical model of field-aligned current patterns. Auroral hiss on the dayside occurs when the auroral oval is centered near the latitude of the station, and in the afternoon sector higher disturbance levels are required. The afternoon sector favors positive B_y when B_z is positive and negative B_y when B_z is strongly negative, while the morning sector favors the complementary conditions. In each case the preference for hiss occurrence follows the pattern of upward field-aligned currents, and hiss is more likely in the configuration where the peak in the upward current is closer to the latitude of the station. IMF B_y does not play a role on the nightside where hiss is most likely to occur during moderately weak driving conditions as higher disturbance levels are expected to move the auroral oval and upward current systems to latitudes well equatorward of South Pole.

1. Introduction

Auroral hiss is an intense whistler-mode radio emission that is a ubiquitous feature of the Earth's auroral zone (see reviews by *Sazhin et al.* [1993] and *LaBelle and Treumann* [2002]) with similar emissions being observed on both Jupiter [*Gurnett et al.*, 1979] and Saturn [*Xin et al.*, 2006]. Auroral hiss generation is tied to the complex physics of the auroral acceleration region. Broadband VLF emissions are produced by both upward and downward propagating electron beams. Upward propagating VLF emissions observed by spacecraft exhibiting a distinct hyperbolic or V-shaped frequency-time structure are referred to as VLF saucers and have been associated with upward electron beams (tens to a few hundreds of eV) in the downward current regions [*Gurnett and Frank*, 1972; *James*, 1976; *Lonnqvist et al.*, 1993; *Ergun et al.*, 2001]. The more generic term auroral hiss refers to both upward and downward propagating broadband VLF emissions that may take on a funnel-shaped or broad V-shaped frequency-time structure when observed by high- or low-altitude spacecraft [e.g., *Gurnett et al.*, 1983; *Gurnett and Frank*, 1972]. The frequency-time structure of broadband VLF emissions has been attributed to propagation near the whistler-mode resonance cone from a spatially localized source (resulting in a saucer) [*Mosier and Gurnett*, 1969; *James*, 1976] or longitudinal sheet source (resulting in a funnel) [*Santolík and Gurnett*, 2002].

Downward propagating auroral hiss is believed to be generated by down going field-aligned electron beams. Auroral hiss on the dayside, often referred to as cusp hiss, has been associated with softer electron precipitation of several hundred eV, while evening sector hiss has been observed in conjunction with more energetic (several keV) inverted-V precipitation events [*Gurnett and Frank*, 1972; *Hoffman and Laaspere*, 1972; *Laaspere and Hoffman*, 1976]. The generation mechanism for auroral hiss is considered to be convective beam amplification, which involves coherent amplification of whistler-mode waves via Landau resonance with the parallel portion of the electron distribution function [*Maggs*, 1976]. Auroral hiss bears no relation to a similarly named emission in the inner magnetosphere, plasmaspheric hiss, which is a known driver of radiation belt electron loss [*Xiao et al.*, 2009, 2010; *Orlova et al.*, 2016]. Auroral hiss is believed to be a consequence of auroral electron acceleration rather than a driver of electron dynamics.

Auroral hiss is observed on the ground although the occurrence rate is significantly reduced compared with spacecraft observations [*Gurnett*, 1966; *Makita*, 1979; *Ungstrup and Carpenter*, 1974]. Ground-based

measurements of VLF waves are limited to the subset of emissions that arrive at the ionospheric boundary with wave normals near vertical. *Sonwalkar and Harikumar* [2000] proposed that the high wave normal auroral hiss emissions could be scattered into the ionospheric transmission cone by meter-scale *F* region density irregularities. In addition, ionospheric absorption, as measured by riometers, influences the ability of auroral hiss to penetrate to the ground. For moderately weak levels of absorption, auroral hiss is positively correlated with absorption, but during strong absorption events, auroral hiss is absent [*Harang and Larsen*, 1965]. Auroral hiss observed on the ground tends to be fairly localized with observations at stations separated by more than several hundred kilometers being uncorrelated [*Jørgensen*, 1966; *Srivastava*, 1976; *Makita*, 1979].

Jørgensen [1966] put together a rough picture of auroral hiss global occurrence by gathering ground observations from 13 stations distributed in latitude and found that hiss occurred in a horseshoe-like pattern (in latitude and magnetic local time (MLT)) extending from ∼17 to 02 MLT with a peak occurrence near 70° magnetic latitude an hour or so before midnight. The local time distribution on the ground is somewhat narrower than observed by spacecraft, see Figure 3 of *Makita* [1979]. Stations at higher latitude (>75°) are more likely to observe hiss near noon and across the afternoon sectors. Near 70°, *Hayakawa et al.* [1975] found that hiss occurrence peaks when the local *K* index was around 5 with occurrence falling off for higher disturbance levels.

A number of studies have explored the connection between auroral hiss and the visible aurora and found the relationship to be complex, see discussion in section 2.3 of *LaBelle and Treumann* [2002]. This is likely due to the multiple factors influencing VLF propagation to the ground, as discussed above, as well as the fact that the two phenomena are generated at different altitudes possibly by different electron populations. In the premidnight sector, impulsive auroral hiss (extending to several hundred kilohertz in frequency and lasting on the order of several minutes) tends to be associated with the expansion phase of auroral substorms when there is an active auroral arc near zenith [*Harang and Larsen*, 1965; *Makita*, 1979; *LaBelle et al.*, 1994]. Continuous auroral hiss (limited to frequencies less than 30 kHz and lasting for tens of minutes to hours) is more likely to be associated with a steady auroral arc and may occur without local magnetometer deflections. Also, the ionospheric exit point of continuous hiss may be latitudinally separated from aurora [*Makita*, 1979].

While the majority of previous ground-based studies have focus on the nightside, recently, *Yan et al.* [2013] examined dayside auroral hiss as observed at South Pole station in both the VLF and LF bands. Although having a lower overall occurrence rate than on the nightside, hiss occurs regularly on the dayside (6–18 MLT) and is divided into prenoon and postnoon populations with a distinct gap at noon. Prenoon hiss was found to be associated with interplanetary magnetic field (IMF) $B_y < 0$ conditions, and this was attributed to the shifting of the field-aligned current patterns. Postnoon hiss was associated with elevated Kp, AE, more strongly negative IMF B_z, and substorm-like conditions as observed in global auroral images, and *Yan et al.* [2013] concluded that the postnoon events may be connected with nightside substorm activity.

Here we use an 8 year database of VLF observations from South Pole station (invariant latitude of −74° with MLT = UT −3.5 h) to examine the variation of auroral hiss as a function of season, magnetic local time, geomagnetic conditions, and interplanetary magnetic field (IMF) conditions. This unprecedentedly large database of observations allows us to examine hiss observations in the context of global magnetospheric configuration. We expand the work of *Yan et al.* [2013] and use empirical models to quantitatively explore the relationship between hiss occurrence, auroral boundaries, and field-aligned current patterns.

2. Auroral Hiss Database

Recordings of VLF wave activity have been made at the geographic South Pole continuously for several decades. The VLF wave receiver consists of two vertical, orthogonal magnetic loop antennas and a preamplifier buried under the antennas [*Harriman et al.*, 2010]. The preamplifier drives a long cable to a line receiver and recording system located inside the nearby station. Typically, broadband data are recorded synoptically; that is, 1 min of data is stored every 15 min, most often at 5, 20, 35, and 50 min after the hour. Historically, the data were recorded on reel-to-reel analog magnetic tapes. While the tapes provide for high-fidelity recordings (up to 24 kHz bandwidth), analyzing the data is somewhat burdensome as the data must first be digitized with rates not faster than twice real time. As such, data analysis tended to focus on event studies [e.g., *Salvati et al.*, 2000; *Sonwalkar and Harikumar*, 2000].

Starting in 2001 at South Pole, it became feasible to record the data digitally, first on compact disk (CD) and later on digital versatile disk (DVD). Both antenna channels are low-pass filtered and sampled at 100 kHz with
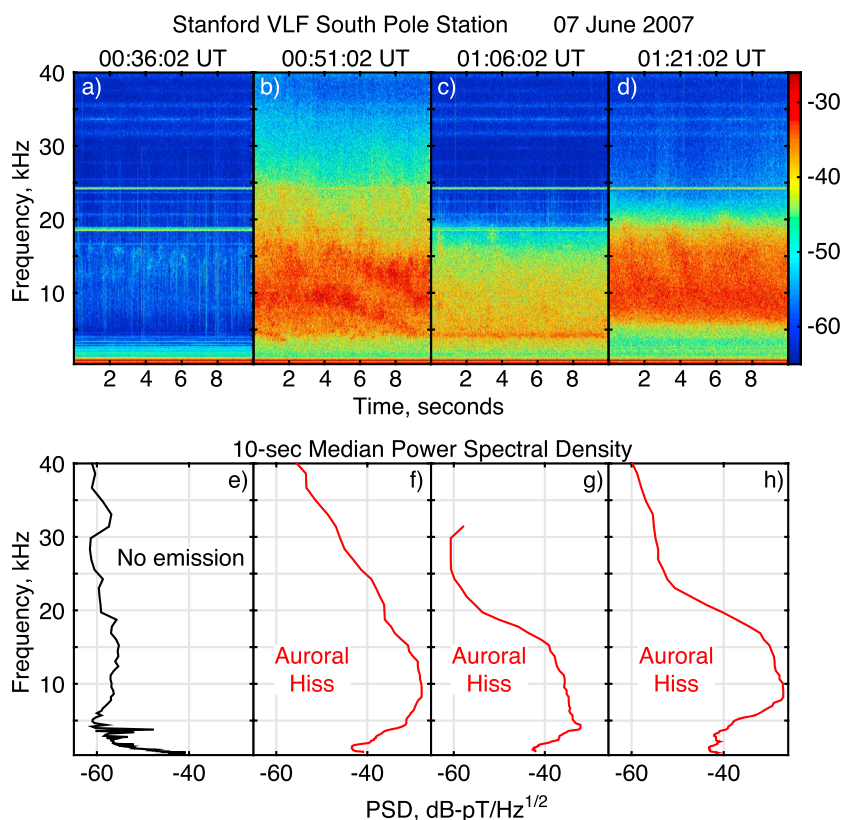
Figure 1. South Pole VLF data from 07 June 2007. (a–d) The 10 s spectrograms from consecutive synoptic intervals. (e–h) The median power spectral density over that 10 s interval. The red curves in Figures 1f–1h indicate that the neural network has identified auroral hiss between the frequency bounds of the curve.

16 bit resolution. Thus, 1 min of synoptic broadband data is about 23 MB. While the digital recording media eases the analysis burden, examining weeks or months of data requires loading a large number of individual disks. In recent years, there have been dramatic increases in capacity and decreases in cost of hard disk drive storage systems. As a result, the digital data from South Pole station from 2001 to 2008 (~4 TB of data) have been transferred from the CDs and DVDs to a hard disk drive-based server. The data server allows for efficient access to the data and facilitates the use of advanced analysis techniques to process and analyze large volumes of data.

Golden et al. [2011] developed a neural network-based algorithm to detect and categorize radio emissions observed in ground-based broadband VLF data based on the spectral characteristics of the data. The neural network was initially trained and applied to 10 years of synoptic data from Palmer Station, Antarctica [*Golden et al.*, 2011] and was later modified and retrained on South Pole data. Neural networks are a machine learning technique used to construct a mapping between an input set of data and an output set of data using a subset of data for which the outputs are known, and this subset is referred to as the training set. For more background on neural networks and application to geophysical data, see *Zhelavskaya et al.* [2016]. In our application, the input data are the median values of the power spectral density (PSD) over a 10 s interval of data in 100 log-spaced frequency bins, and the outputs of the model are the type and frequency extent (upper and lower cutoff) of each emission present in the data interval. In the South Pole data, the algorithm identifies two emissions of magnetospheric origin, chorus, and auroral hiss. A median value of the PSD is used rather than an average to minimize the contribution of impulse signals such as radio atmospherics (sferics) from distant lightning sources. Log-spaced frequency bins are used in order to resolve chorus, which at South Pole tends to be limited to below 2 kHz, while also covering the full frequency range of auroral hiss, up to 50 kHz. The training set of known output data was constructed by manually identifying the emissions for 1 day out of each month of data available. Considering 8 years of data and 96 synoptic intervals per day, the training set for South Pole consisted of 9616 profiles of the PSD as input and the manually identified emissions for
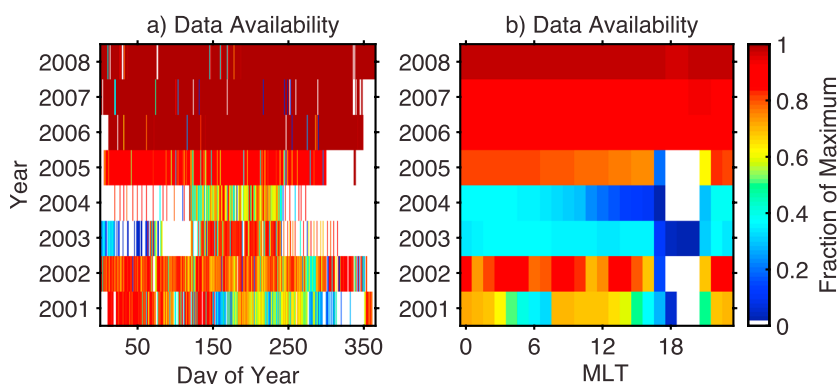
Figure 2. The availability of South Pole data as a fraction of the maximum possible (assuming four synoptic intervals per hour, 24 h per day) as a function of (a) year and day of year and (b) year and MLT.

each profile as output. Once the neural network was trained, validated, and tested using the training set, it was applied to the remaining 172,111 synoptic intervals available to automatically identify the emissions. The database of chorus emissions from South Pole was analyzed as part of *Spasojevic* [2014]. Some analysis of the auroral hiss database from South Pole was presented in *Yan et al.* [2013], and here we provide a more in-depth analysis. The auroral hiss database consists of the universal time of the event in 15 min increments, the power spectral density in 100 log-spaced frequency bins averaged over a 10 s segment of data, and the upper and lower frequency cutoffs of the emission.

Figure 1 shows an example of South Pole data for an interval when auroral hiss was detected. Figures 1a–1d show 10 s spectrograms from four consecutive synoptic intervals and Figures 1e–1h show the median PSD profile. The neural network algorithm identified the presence of auroral hiss in three of the PSD profiles, and the red curves indicate the identified upper and lower frequency cutoff of the emission. No emission was detected in the first interval.

From 14 January 2001 to 31 December 2008, there are 279,264 potential synoptic intervals assuming four synoptic intervals per hour and 24 h per day of recordings. We have data available for 181,327 intervals, yielding 65% data coverage. Figure 2 shows the fraction of data available as a function of (a) year and day of year and (b) year and magnetic local time (MLT). Years 2006 through 2008 have the highest data coverage at >90%. Years 2003 (30%) and 2004 (24%) have the lowest data coverage, and unfortunately, this is attributed to low-quality writable DVDs that were used in those years. The inconsistent coverage as a function of year makes it difficult to analyze auroral hiss trends as a function of year or solar cycle phase. Further, data coverage tends to be low in the month of December (day of year >335) since the system undergoes maintenance and repairs at that time. In Figure 2b, we can see that from 2001 to 2005, there is a gap in data coverage from 18 to 21 MLT. In those years, the same computer that was used to digitize the data was also used to burn the recordable media, and it was necessary to pause the recordings to perform this task. Unfortunately, this local time interval coincides with a high occurrence of auroral hiss. Therefore, it is important to note that most all events from 18 to 21 MLT come from 2006 to 2008. There are a total of 14,018 auroral hiss events available for analysis. In this work, we do not attempt to differentiate between continuous and impulsive auroral hiss, and such analysis is left for future work.

3. Day-Night Effects

VLF waves generated in the magnetosphere must propagate through the lossy ionosphere in order to be observed on the ground. Transionospheric absorption of VLF waves primarily depends on the angle of the magnetic field and the electron density and collision frequency profile in the *D* region ionosphere at 60 to 90 km altitude. At the geographic South Pole, day and night ionospheric conditions are annual rather than diurnal with the sunset at 100 km altitude occurring around 15 April each year and sunrise around 27 August. Figure 3a shows how the normalized occurrence of auroral hiss at South Pole varies by month of year. There is a clear increase in occurrence for nighttime ionospheric (low-density) conditions. Overall, auroral hiss occurs in about 10% of synoptic intervals at night and 6% during the day. Similarly, auroral hiss amplitude is higher at night as seen in Figure 3b. Under daytime ionospheric conditions, auroral hiss amplitudes tend to minimize
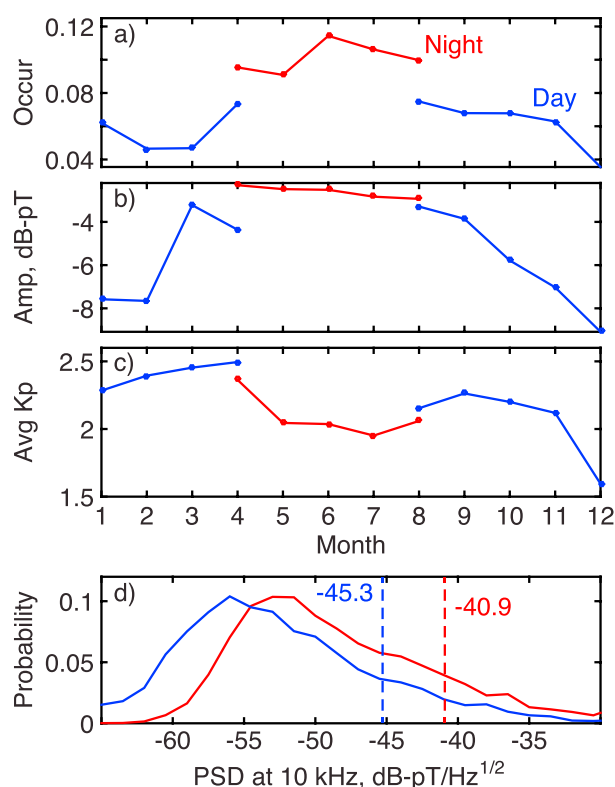
Figure 3. Day-night effects in auroral hiss observations. (a) The occurrence of auroral hiss, (b) the average amplitude, and (c) the average Kp during auroral hiss intervals as a function of month of year for daytime (blue) and nighttime (red) ionospheric conditions. (d) The probability distribution of power spectral density at 10 kHz for day (blue) and night (red) with the dashed lines indicating the mean value of the distribution.

in the months surrounding southern summer solstice (December) suggesting a further seasonal influence on ionospheric absorption. We note that the International Reference Ionosphere (IRI-2007) [*Bilitza and Reinisch*, 2008] does not predict seasonal variation below 92 km under daytime conditions at South Pole although this is likely due to a lack of abundant measurements of the D region ionosphere.

Figure 3c shows the average value of Kp during auroral hiss observations. The average Kp tends to be lower for night events than day events. This suggests that due to increased ionospheric absorption during the day, we can only observe auroral hiss events that occur during stronger geomagnetic disturbances and presumably have higher amplitude near the source region. In contrast at night there is less absorption, and we can observe weaker hiss events that occur during weaker disturbances.

Finally, in Figure 3d, we examine the probability distribution of the auroral hiss power spectral density (PSD) at 10 kHz, which is near the peak of the emission spectrum. More large PSD events are observed at night, and the mean value of the PSD is about 4.4 dB higher for night versus day. This difference is consistent

with expectations from updated calculations of transionospheric absorption performed by *Graf et al.* [2013] that show differences in attenuation between day and night at this geomagnetic latitude to be on the order of 4 to 8 dB depending on ionospheric conditions.

On the other hand, Figure 3d shows that there are fewer low PSD measurements at night than during the day. This trend is not expected from transionospheric propagation and instead may be the result of contaminating subionospheric signals. Under nighttime ionospheric conditions, VLF waves can travel for long distances in the Earth-ionosphere waveguide with very little attenuation, on the order of a few decibels per 1000 km [*Walker*, 1974; *Tsuruda et al.*, 1982], and as a result, more sferics from distant lightning sources are observed at South Pole at night. The wave energy from sferics essentially raises the noise floor at night in the frequency range from about 2 kHz to about 20 kHz, and the automatic emission detector can only observe auroral hiss with amplitude higher than this noise floor. During the day a lack of contaminating sferic energy results in the ability to detect hiss events that have weaker signatures at ground level (although the results of Figure 3c suggest that the source region amplitudes for the daytime emissions must be higher in order to survive the transionospheric attenuation).

4. Variation With Magnetic Local Time

Next, we examine the MLT distribution of auroral hiss as observed at South Pole. Figure 4a shows the normalized occurrence of auroral hiss as a function of MLT. This is similar to Figure 3 of *Yan et al.* [2013], but here we separately plot occurrence for all data (black), nighttime ionospheric conditions (red), and daytime (blue). As noted in the previous section, because the station is located at the geographic south pole, day-night ionospheric conditions and MLT are independent. That is, there are the same number of hours of daylight at 12 MLT
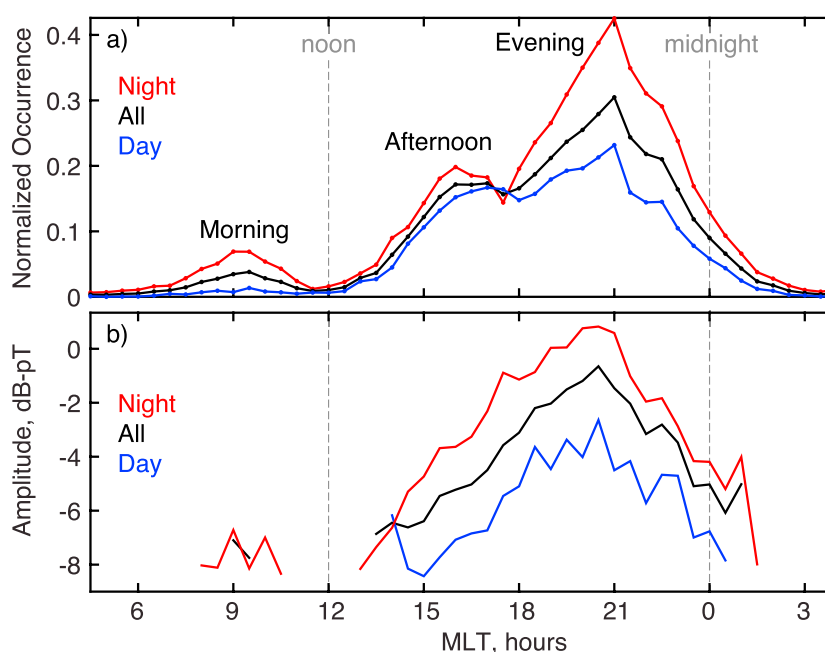
Figure 4. The magnetic local time distribution of auroral hiss (a) normalized occurrence and (b) average amplitude for all observations (black), nighttime (red), and daytime (blue) ionospheric conditions. In Figure 4a, three local time occurrence peaks are identified and labeled as morning, afternoon, and evening.

as there are at 24 MLT. Figure 4b shows the average amplitude of auroral hiss for local times where the hiss occurrence exceeds 3%. As was discussed in *Yan et al.* [2013], there are three distinct peaks in occurrence with local time. First, in the morning sector there is a population of auroral hiss that is centered at 9 MLT. Morning sector hiss is observable only during nighttime ionospheric conditions with a peak occurrence of 7% and low average amplitude. Morning sector hiss is followed by a minimum in occurrence that is centered about a half hour before local noon. In the afternoon sector, there is a local maximum in occurrence that during nighttime is centered at 16 MLT with a maximum occurrence of 20%. The afternoon peak and subsequent local minimum is shifted to slightly later local times during daylight conditions. The overall maximum in hiss occurrence, 43% at night, is centered at 21 MLT and does not appear to shift under daylight conditions. The existence of the local minimum between the peaks in occurrence (Figure 4a) in the afternoon and evening sectors suggests that the hiss in the two sectors may result from different driving conditions. On the other hand, when examining average amplitude instead of occurrence (Figure 4b), the average amplitude maximizes in the evening sector and does not exhibit a local minimum near dusk. Finally, there is an absence of hiss across the early morning hours with <3% occurrence from about 2 to 7 MLT.

Across the afternoon and evening sectors, the average difference in amplitude between day and night observations is fairly steady at about 4 dB. However, the difference in night and day occurrence is a factor of about 2 in the evening and only about 1.4 times in the afternoon. This may be related to the issue discussed in relation to Figure 3d where the minimum detectable amplitude at night is higher due to a higher VLF noise floor. Particularly, in the afternoon sector, there are fewer events detected during the night with low amplitude, and while this does not strongly influence the average amplitude (which is dominated by the high amplitude events), it does reduce the afternoon nighttime occurrence rate.

5. Relation to *Kp* and Aurora Boundaries

Next we examine the relationship between the occurrence of hiss and a model of the auroral boundaries by *Carbary* [2005]. The *Carbary* [2005] model provides the magnetic latitude of the poleward edge, the equatorward edge, and the peak intensity of the auroral oval as a function of MLT and Kp. The model is based on northern hemisphere global images from the Polar Ultraviolet Imager [*Torr et al.*, 1995].

Since the auroral boundary model is based on *Kp*, we first examine the occurrence of auroral hiss as a function of *Kp*. Figures 5a – 5d shows the normalized occurrence of auroral hiss at South Pole in four local time sectors,
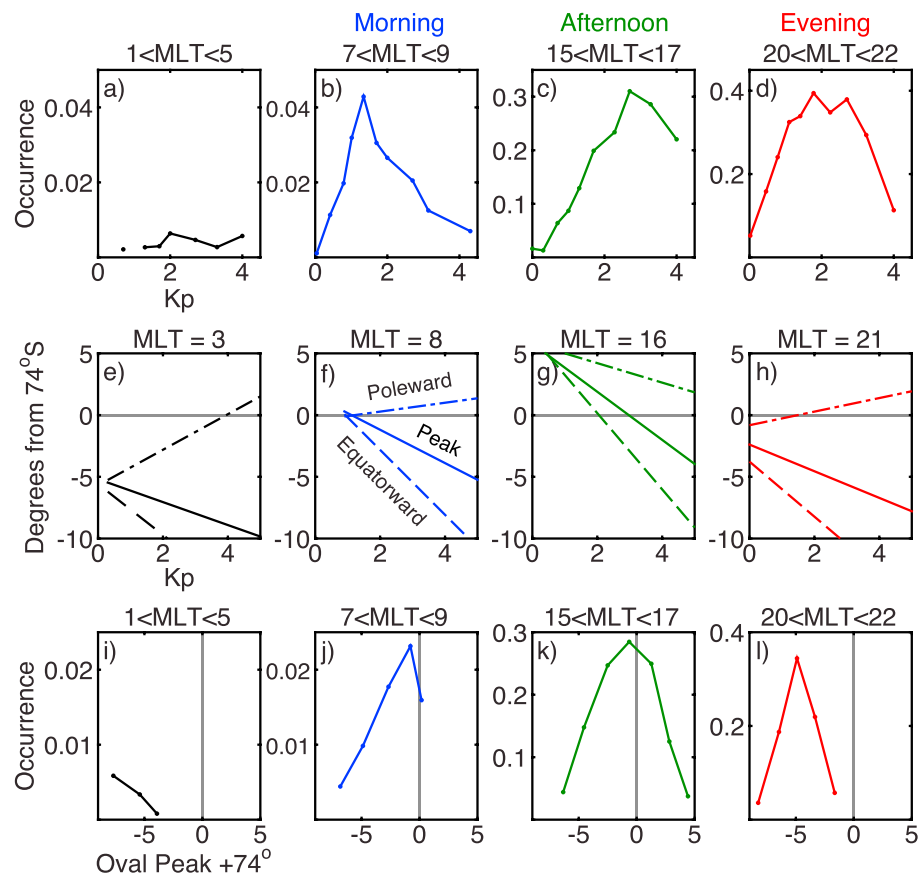
Figure 5. Relationship among auroral hiss occurrence, *Kp*, and the auroral boundaries. (a–d) The normalized occurrence of hiss as a function of *Kp* in four local time sectors. (e–h) The location of the poleward (dash-dotted) and equatorward (dashed) auroral boundary and the peak precipitation (solid) as a function of latitude away from South Pole station (positive values are poleward) at the center of each local time sector. (i–l) Occurrence of hiss as a function of the latitudinal distance between the auroral peak precipitation and the latitude of South Pole (positive values indicate the auroral peak is poleward of the station).

(a) 1 < MLT < 5 where hiss is rarely observed, (b) morning, (c) afternoon, (d) evening. The morning sector is chosen as 7 < MLT < 9 rather than centered on the local maximum in occurrence (8 < MLT < 10) since the *Carbary* [2005] model is not defined on the dayside in the range of 9 to 13 MLT. For 1 < MLT < 5 (Figure 5a), hiss occurrence is low at <1% for all levels of *Kp*. In the morning sector (Figure 5b), hiss occurrence peaks at relatively low *Kp* levels, 1⁺, and falls off for increasing *Kp*. In contrast, in the afternoon sector (Figure 5c) hiss tends to occur at much higher *Kp* levels with a peak at *Kp* of 3⁻. *Yan et al.* [2013] also reported on average higher *Kp* values for afternoon sector hiss. In the evening sector (Figure 5d), there is high hiss occurrence over a broader range of *Kp* from 1 to 3⁺.

Figures 5e–5h show the output of the *Carbary* [2005] model evaluated at the center of the local time bin in each column. The output of the model has been centered about the latitude of South Pole, such that positive values indicate latitudes poleward of the station and negative values indicate latitudes equatorward. At MLT = 3 (Figure 5e), the auroral boundaries are significantly equatorward of the station for the entire range *Kp*, consistent with the lack of auroral hiss is this sector. At MLT = 8 (Figure 5f), the auroral boundaries are not defined for the lowest *Kp* values, when hiss occurrence is also low. The auroral boundaries are centered near the station at *Kp* values when hiss occurrence peaks. The auroral boundaries move to latitudes equatorward of the station for higher *Kp* when hiss occurrence also falls off. At MLT = 16 (Figure 5g), the auroral boundaries are well poleward of the station for low *Kp* and move equatorward toward the station for moderate values of *Kp* when hiss occurrence also peaks. At MLT = 21 (Figure 5h), the peak of auroral oval is equatorward of the station for all values of *Kp*, but the oval is significantly broader than in the morning and afternoon sectors, which may correspond to the occurrence of hiss over a broader range of *Kp*. Also, the peak precipitation,
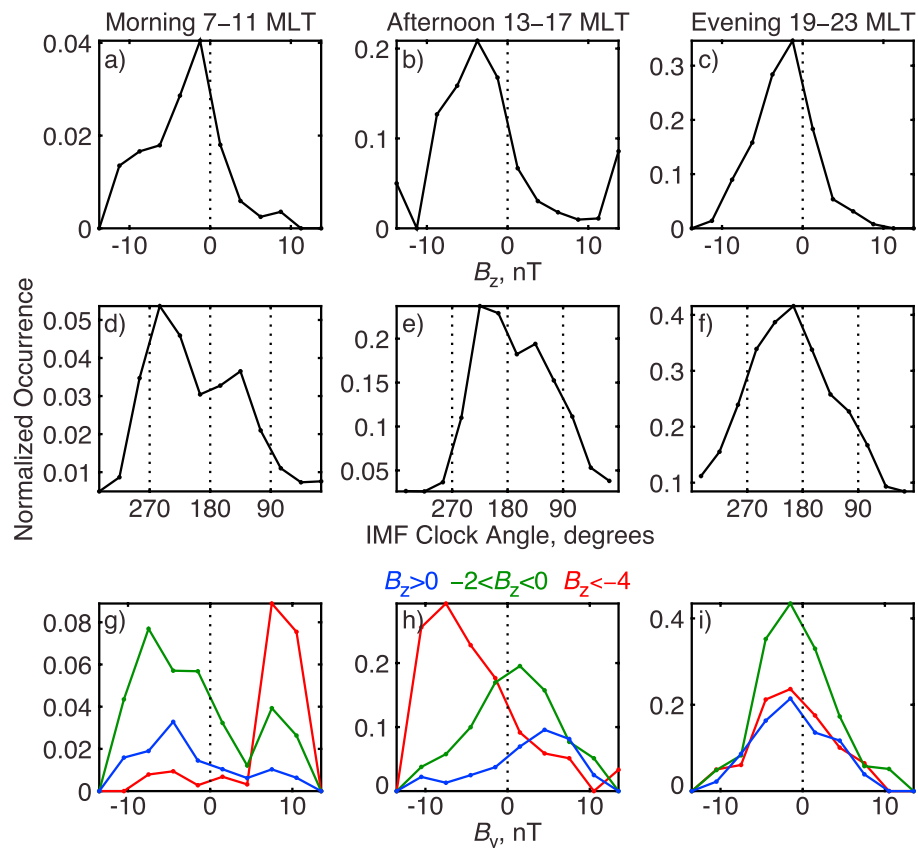
Figure 6. The normalized occurrence of auroral hiss in three local time sectors with respect to (a–c) IMF B_z, (d–f) IMF clock angle, and (g–i) IMF B_y. In Figures 6g–6i, the blue curve limits the data to $B_z > 0$, the green curve limits the data to $-2 > B_z > 0$, and the red curve limits data to $B_z < -4$ nT.

another output of *Carbary* [2005] model but not plotted here, is significantly higher in the evening than in the morning and afternoon sectors for all levels of *Kp*.

Figures 5i–5l combine and recast the data from Figures 5a–5d and Figures 5e–5h and plot the normalized occurrence of hiss as a function of distance between the peak of the auroral oval and the observing station where negative values indicate that the peak of the oval is equatorward of the station and positive is poleward. For the morning and afternoon sectors (Figures 5j and 5k), hiss occurrence is maximized when the auroral oval is centered above the station. For the evening sector (Figure 5l), auroral hiss occurrence maximizes when the peak of the oval is about 5° equatorward of the station.

6. Relation to IMF Strength and Direction

In this section, we examine the occurrence of auroral hiss at South Pole as a function of the strength and direction of the tangential component of the interplanetary magnetic field (IMF). For analysis in Figure 6, we calculate the average values of the IMF for the one hour preceding the hiss observation. We also performed the analysis using half-hour averages and found essentially identical results. Figures 6a–6c show the normalized occurrence of auroral hiss as a function of IMF B_z for the morning, afternoon, and evening sectors. All sectors favor southward IMF with the afternoon sector shifted to more strongly negative values of B_z compared with morning or evening, consistent with occurrence in the afternoon also favoring higher *Kp* (Figure 5c).

Figures 6d–6f show the normalized occurrence of auroral hiss as a function of IMF clock angle, θ, defined as $\theta = \tan^{-1}(B_y/B_z)$. For all three local time sectors, hiss can occur over a broad range of clock angles from 90° to 270°, but the peak occurrence is in the range of 180° to 270°, that is, for $B_z < 0$ and $B_y < 0$. Putting together Figures 6a and 6d, morning sector hiss is most likely to occur under modest and negative B_y-dominated IMF. Afternoon sector hiss favors stronger driving with $\theta = 225°(-45°)$, and evening sector hiss favors weakly negative IMF.

We note that the results for the afternoon sector contradict that of *Yan et al.* [2013]. Using superposed epoch analysis, *Yan et al.* [2013] shows that both VLF and LF auroral hiss are more likely to occur in the afternoon sector when $B_y > 0$. We believe that the difference between *Yan et al.* [2013] and the results in Figure 6e is that we have normalized the occurrence rate based on how often that value of IMF was observed. If we examine value of B_y for all afternoon events, we find that both the mean and median value of B_y is >0. However, in Figure 6e, we normalized the occurrence rate by dividing the number of events in each bin by the number of total observations in that bin, and in that case we find that the afternoon sector has a slight overall preference for $B_y < 0$.

In Figures 6g–6i, we take the analysis one step further and examine the distribution of IMF B_y for three different ranges of IMF B_z: positive ($B_z > 0$, blue), weakly negative ($-2 < B_z < 0$, green), and strongly negative ($B_z < -4$, red). The occurrences are all normalized; that is, each dot represents the number of events for that level of B_y and B_z divided by the number of observations of that level of B_y and B_z in the data set. Starting first with the evening sector (Figure 6i), we find that the distribution of B_y is essentially independent of B_z. All three curves have a similar shape peaking for slightly negative values of B_y and falling off with higher values of B_y.

This is not the case for the morning and afternoon sectors. In the morning sector, when B_z is positive and hiss occurs, B_y tends to be negative (Figure 6g, blue curve). When B_z is strongly negative and hiss occurs, B_y dramatically shifts to positive values (Figure 6g, red curve). Weakly negative B_z (green curve) represents a transition between these two states with significant occurrence for both negative a positive values of B_y. The opposite effect is seen in the afternoon sector (Figure 6h) where hiss occurs for positive B_y when B_z is positive (blue curve), and hiss occurs for negative B_y when B_z is strongly negative (red curve), with weakly negative B_z producing something in between (green curve).

7. Relation to Upward Current Regions

In order to understand the connection between IMF driving conditions and auroral hiss occurrence, we utilize an advanced, high-resolution, empirical model of the field-aligned current systems developed by *He et al.* [2012]. The *He et al.* [2012] model of FACs through empirical orthogonal function analysis (MFACE) is based on 10 years of data from the Challenging Minisatellite Payload and provides the field-aligned current density at 110 km as a function of geomagnetic latitude, MLT, day of year, and solar wind driving conditions. For the runs presented below, we set the day of year to 171 (near the peak of hiss occurrence) and vary the latitude, MLT and IMF B_z and B_y allowing the other parameters to revert to their default values. We note that on day 171, the station is under nighttime ionospheric conditions. We also performed the same analysis using different values of day of year to consider daytime ionospheric conditions. Under daytime conditions, the intensity of the FACs are somewhat higher, and some of the current structures shift slightly in latitude, but the overall trends that we emphasize in our analysis below still hold.

In Figure 7a, we examine the field-aligned current density as a function of latitude at MLT = 9. The dashed black curve is the output of MFACE using the median values of IMF B_z and B_y for all observation intervals (with or without hiss occurrence) in the morning sector (7 < MLT < 11), that is, $B_z = 0.1$ and $B_y = 0$ nT. For these weak driving conditions, we can see upward currents at high latitude followed by downward region 1 (R1) currents with the upward region 2 (R2) system being absent. The thick blue curve in Figure 7a is the output of MFACE using the IMF conditions for which hiss is most likely to occur in the morning sector. These IMF values are taken from the peaks in the normalized distributions in Figures 6a and 6d and correspond to $B_z = -1.3$ and $B_y = -4.7$ nT. In this case, there are clear strong downward R1 currents followed by upward R2 currents. The peak upward R2 current density map slightly equatorward of South Pole station (vertical gray line). Further, increasing the strength of the IMF moves the R2 system further equatorward of South Pole.

Figure 7b shows a similar plot using the MFACE at MLT = 15. The dashed black curve uses the median driving conditions in the afternoon sector (13 < MLT < 17), and we can see downward currents at high latitude followed by the upward R1 with the downward R2 being absent. For driving conditions when hiss is most likely to occur (thick, blue curve), there are stronger upward R1 currents with a peak density located just poleward of the station. The magnitude of the upward current density is stronger in the afternoon sector than the morning sector. If we weaken the IMF, the duskside R1 current system moves to latitudes poleward of the station.

In the evening sector at MLT = 21 (Figure 7c), under the median conditions (black dashed line) a clear upward R1 and downward R2 system is seen at latitudes equatorward of the station. For conditions when hiss is more
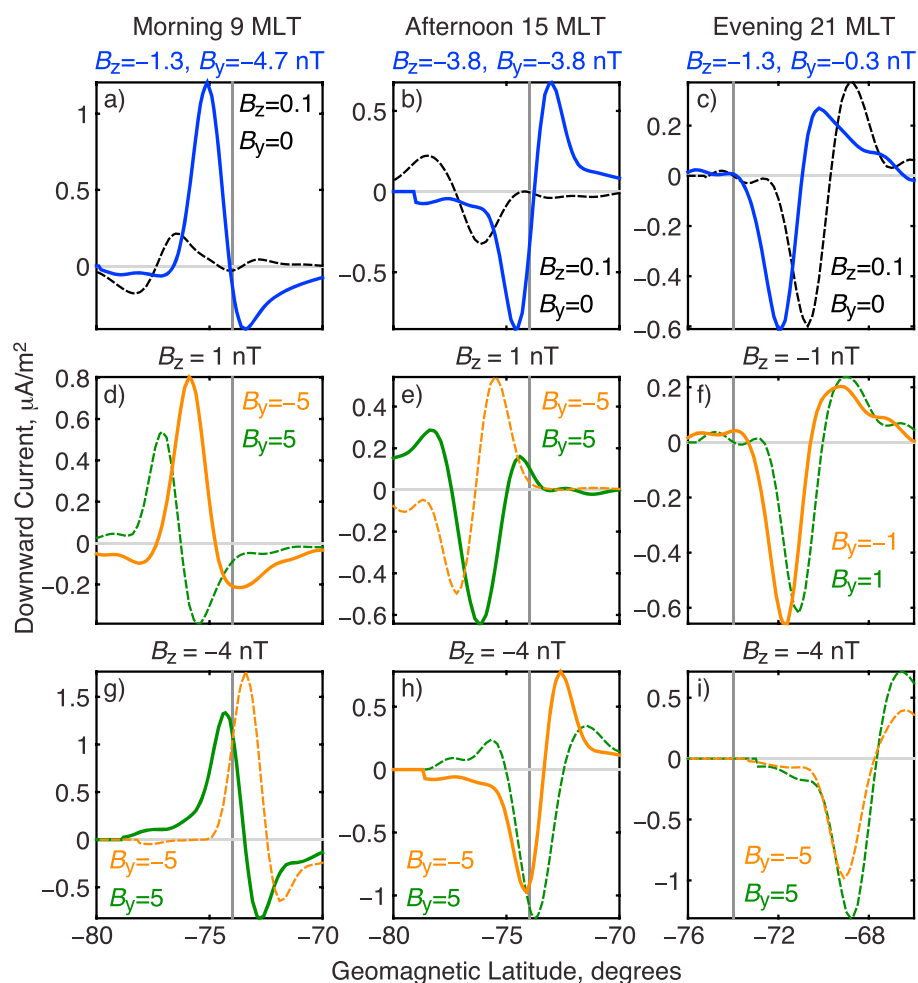
Figure 7. Downward field-aligned current density as a function of latitude from a model of field-aligned currents (FACs) through empirical orthogonal functions analysis (MFACE) at three different local times (columns) with each panel comparing two different configurations of IMF B_z and B_y. Configurations for which auroral hiss is more likely to occur are plotted with a thick, solid line, and configurations for which hiss is less likely to occur are plotted with a dashed line.

likely to occur (blue line), the current pattern is shifted to higher latitude with the upward R1 currents being closer to the station. Thus, we find that in all three local time sectors, hiss is more likely to occur when the upward current system is present and located at latitudes closer to the station than under median driving conditions.

Now we explore motion of the FAC systems with the direction of B_y and the relation to hiss occurrence. In Figure 7d, we present the output of MFACE at MLT = 9 using weak northward IMF ($B_z = 1$ nT) and both negative (orange) and positive (green) values of B_y with a magnitude of 5 nT. The negative B_y (orange) curve has been thickened to indicate that these are conditions for which hiss is more likely to occur (see blue curve in Figure 6g), and the positive B_y (green) curve has been dashed to indicate that hiss is less likely to occur. We find that for negative B_y the upward R2 currents peak at a latitude very close to South Pole.

Next, we continue to look at the morning sector but examine moderately strong southward IMF ($B_z = -4$ nT) in Figure 7g. Under the stronger driving conditions the current systems have move to lower latitude. However, under positive B_y (green) conditions the upward R2 currents are closer to the station, and these are also the conditions for which hiss is more likely to occur at South Pole (see red curve in Figure 6g).

Similar plots for the afternoon sector at MLT = 15 are shown for $B_z = 1$ nT in Figure 7e and $B_z = -4$ nT in Figure 7h. In both cases, we also find that the conditions for which hiss is more likely to occur

(thick, solid lines) are also the conditions for which the upward R1 current system is closer in latitude to the station. This corresponds to positive B_y (green) for positive B_z (refer to blue curve in Figure 6h) and negative B_y (orange) for negative B_z (red curve in Figure 6h).

For auroral hiss occurring in the evening sector, there is a preference for slightly negative B_y for all levels of B_z (all three curves in Figure 6i), so in Figure 7f we explore slightly different scenarios for MLT = 21. In Figure 7f, we set B_z to weakly negative (when hiss occurrence maximizes overall) and look at the current pattern for weakly negative B_y (orange) and weakly positive B_y (green). Again, we see that weakly negative B_y (orange) brings the upward R1 currents slightly closer to South Pole, and those conditions favor the occurrence of hiss (green curve in Figure 6i).

Finally, in Figure 7i, we look at evening sector currents under moderately strong southward IMF ($B_z = -4$ nT). For both polarities of B_y, the upward current system is well equatorward of South Pole, and also, the overall probability of hiss occurrence is significantly reduced for these stronger driving conditions (Figures 6c and 6i).

In summary, we find considerable agreement between the latitudinal distribution of upward field-aligned currents and the occurrence of auroral hiss. For each scenario tested in Figure 7, we find that the probability of hiss occurrence is higher for the configuration which brings the upward current system (R2 in the morning sector, R1 in the afternoon and evening sectors) closer in latitude to the observing station.

8. Discussion

A database of 14,018 auroral hiss events was derived from 8 years of VLF observations at South Pole station. We used this database to examine the seasonal, MLT, Kp, and IMF dependence of auroral hiss. We used empirical models of the auroral boundaries and the field-aligned current distribution to understand the differences in auroral hiss occurrence as a function of local time.

The occurrence and amplitude of auroral hiss are higher under nighttime ionospheric conditions consistent with expectations from reduced ionospheric absorption during nighttime transionospheric propagation (Figures 3a and 3b). We observe a further seasonal effect with hiss occurrence maximizing near winter solstice and minimizing near summer solstice (Figures 3a and 3b) that we attribute seasonal changes in the ionospheric electron density profile but which are not captured in the standard IRI model. Auroral hiss events observed during the day tend to occur during periods of stronger geomagnetic activity as indicated by the Kp index (Figure 3c), which is consistent with the idea that higher amplitudes near the source region are needed to survive the higher absorption during the day.

Auroral hiss is observed on 75% of days for which data is available. There are three distinct local times sectors with enhanced hiss occurrence with an overall maximum in hiss occurrence and amplitude at 21 MLT (referred to as evening sector hiss) and local maximums centered near 16 MLT (afternoon hiss) and 9 MLT (morning hiss).

There is a broad minimum where hiss occurrence is < 3% from 2 to 7 MLT. The Kp-dependent model of auroral boundaries by *Carbary* [2005] indicates that in this local time sector, the auroral oval tends to be well equatorward of the station with the poleward edge of the oval reaching South Pole only for $Kp > 4$ (Figure 5e). Similarly, the *He et al.* [2012] empirical model of field-aligned currents places the peak of the upward R2 system about 5° equatorward of South Pole for $B_z = 1$ nT and 7° equatorward for $B_z = -4$ nT (not shown).

Morning sector auroral hiss at South Pole is only observable during nighttime ionospheric conditions and has an overall low occurrence and average amplitude compared with the afternoon and evening sectors. In the morning sector under quiet geomagnetic conditions ($Kp < 1-$, tangential component of the IMF near zero), the auroral oval is poorly defined (Figure 5f), the upward R2 current system is absent (Figure 7a, black dashed curve), and hiss occurrence is low (Figure 5b). Occurrence in the morning sector is sharply peaked during weakly disturbed geomagnetic conditions, $Kp = 1+$, when the auroral oval is centered above the station. Further, morning sector hiss is mostly likely to occur when B_z is weakly negative and B_y is negative and dominate (Figures 6a and 6d). Under these conditions, the upward R2 system is well defined and the peak current density is close to the latitude of the station (Figure 7a, blue solid curve). As Kp increases further or B_z becomes more strongly negative, the auroral oval (Figure 5f) and the upward R2 currents (Figure 7g) move equatorward of the station and auroral hiss occurrence decreases (Figures 5b and 6a).

Analogously, auroral hiss in the afternoon is more likely to occur when the auroral oval and the upward current system (in this case the R1 currents) are centered near the latitude of the station. However, higher geomagnetic activity and stronger IMF driving conditions are required for this to occur. Under quiet and moderate activity, the auroral oval and the upward R1 currents are well poleward of the station (Figures 5g and 7b, black dashed curve), and hiss occurrence is low (Figure 5c). Under higher geomagnetic activity and stronger IMF driving, the auroral oval and the upward R1 currents move equatorward and are centered closer to the station (Figures 5g and 7b, blue solid curve and 7h, both curves), and hiss occurrence maximizes (Figures 5c and 6b).

Our conclusions about afternoon sector hiss differ from that of *Yan et al.* [2013]. They concluded that since afternoon sector hiss (referred to as postnoon hiss) occurred during elevated Kp and AE conditions and strongly negative IMF B_z, it was connected with nightside substorm activity. We find that afternoon hiss is related to the dayside configuration of the magnetosphere and conditions that bring the auroral oval and upward R1 currents to the latitude of South Pole.

The direction of IMF B_y plays a significant role in determining the occurrence of auroral hiss in both the morning and afternoon sectors. When B_z is positive, hiss is significantly more likely to occur in the morning sector when B_y is negative (Figure 6g, blue curve) and in the afternoon sector when B_y is positive (Figure 6h, blue curve). Contrarily, when B_z is strongly negative, hiss is significantly more likely to occur in the morning sector when B_y is positive (Figure 6g, red curve) and in the afternoon sector when B_y is negative (Figure 6h, red curve). In each case the preference for hiss occurrence follows the pattern of upward field-aligned current distribution, and hiss is more likely in the configuration where the peak in the upward current is closer in latitude to the station. On the other hand, hiss in the evening sector has a preference for weakly negative B_y for all levels of B_z.

As was previously reported in *Yan et al.* [2013], the gap in auroral hiss occurrence between the morning and afternoon sectors is consistent with the midday gap in the discrete auroral oval [*Dandekar and Pike*, 1978], which is shifted about half an hour toward the morning sector [*Newell et al.*, 2005] similar to the hiss occurrence pattern.

The evening sector has the highest overall occurrence of auroral hiss, and hiss occurs on 55% of days in the local time sector between 19 and 22 MLT. Hiss occurrence is elevated over a wider range of Kp than in the morning or afternoon sectors (Figure 5d). The *Carbary* [2005] model of the auroral boundaries indicates that hiss is most likely to occur when the peak precipitation in the auroral oval is located about 5° equatorward of the station (Figure 5l). Similarly, the upward R1 currents tend to be several degrees equatorward of the station for conditions when hiss is most likely to occur (Figure 7c, blue solid curve). The auroral oval is broader in latitude in the evening sector, and the station is within the poleward edge of the oval when hiss occurrence is high (Figure 5h).

The empirical models of the auroral boundaries and field-aligned currents used here present a static picture of the phenomena neglecting the most dynamic behavior that occurs in the evening sector, the auroral substorm. Given that South Pole station tends to be located near the poleward edge of the auroral oval when hiss is likely to occur, it is possible that auroral hiss in the evening sector is at times associated with the westward traveling surge [*Akasofu et al.*, 1965, 1966]. Occurring during the substorm expansion phase, the westward traveling surge is a bulge of discrete auroral that expands both poleward and westward in the evening sector oval. The westward traveling surge is associated with the upward field-aligned current at the duskward edge of the substorm current wedge [*Akasofu and Meng*, 1969; *Kamide and Akasofu*, 1975; *Hoffman et al.*, 1994]. During intervals of high geomagnetic activity, the auroral oval may be significantly expanded such that the westward traveling surge remains equatorward of South Pole, consistent with the decrease in hiss occurrence at high Kp (Figure 5d) and strongly southward IMF (Figure 6c).

9. Summary

In conclusion, using a large database of auroral hiss observations from South Pole, we find that auroral hiss on the dayside is most likely to occur when the auroral oval is centered near the latitude of the station. Morning sector hiss is consistent with the pattern of upward R2 field-aligned currents, and afternoon sector hiss is consistent with the pattern of upward R1 currents. Both the morning and afternoon sector hiss are responsive to changes in solar wind IMF B_y, favoring conditions that bring the peak of the upward current closer to the

station. Auroral hiss on the evening sector is frequently observed at South Pole and may be related to the latitudinally broad region of auroral precipitation in this sector and at times to the poleward expansion of the discrete aurora during substorm expansion phase during weak to moderate disturbance intervals.

References

Akasofu, S.-I., and C.-I. Meng (1969), A study of polar magnetic substorms, *J. Geophy. Res.*, 74, 293–313, doi:10.1029/JA074i001p00293.

Akasofu, S. I., D. S. Kimball, and C.-I. Meng (1965), The dynamics of the aurora—II. Westward traveling surges, *J. Atmos. Terr. Phys.*, 27, 173–174, doi:10.1016/0021-9169(65)90114-5.

Akasofu, S. I., C. I. Meng, and D. S. Kimball (1966), Dynamics of the aurora—IV, *J. Atmos. Terr. Phys.*, 28, 489–496, doi:10.1016/0021-9169(66)90058-4.

Bilitza, D., and B. W. Reinisch (2008), International reference ionosphere 2007: Improvements and new parameters, *Adv. Space Res.*, 42, 599–609, doi:10.1016/j.asr.2007.07.048.

Carbary, J. F. (2005), A *Kp*-based model of auroral boundaries, *Space Weather*, 3, S10001, doi:10.1002/2005SW000162.

Dandekar, B. S., and C. P. Pike (1978), The midday, discrete auroral gap, *J. Geophy. Res.*, 83, 4227–4236, doi:10.1029/JA083iA09p04227.

Ergun, R. E., C. W. Carlson, J. P. McFadden, R. J. Strangeway, M. V. Goldman, and D. L. Newman (2001), Electron phase-space holes and the VLF saucer source region, *Geophys. Res. Lett.*, 28, 3805–3808, doi:10.1029/2001GL013024.

Golden, D., M. Spasojevic, and U. S. Inan (2011), Determination of solar cycle variations of midlatitude ELF/VLF chorus and hiss via automated signal detection, *J. Geophy. Res.*, 116, A03225, doi:10.1029/2010JA016193.

Graf, K. L., N. G. Lehtinen, M. Spasojevic, M. B. Cohen, R. A. Marshall, and U. S. Inan (2013), Analysis of experimentally validated trans-ionospheric attenuation estimates of VLF signals, *J. Geophys. Res. Space Physics*, 118, 2708–2720, doi:10.1002/jgra.50228.

Gurnett, D. A. (1966), A satellite study of VLF hiss, *J. Geophy. Res.*, 71, 5599–5615, doi:10.1029/JZ071i023p05599.

Gurnett, D. A., and L. A. Frank (1972), VLF hiss and related plasma observations in the polar magnetosphere, *J. Geophy. Res.*, 77, 172–190, doi:10.1029/JA077i001p00172.

Gurnett, D. A., W. S. Kurth, and F. L. Scarf (1979), Auroral hiss observed near the Io plasma torus, *Nature*, 280, 767–770, doi:10.1038/280767a0.

Gurnett, D. A., S. D. Shawhan, and R. R. Shaw (1983), Auroral hiss, *Z* mode radiation, and auroral kilometric radiation in the polar magnetosphere: DE 1 observations, *J. Geophy. Res.*, 88, 329–340, doi:10.1029/JA088iA01p00329.

Harang, L., and R. Larsen (1965), Radio wave emissions in the VLF-band observed near the auroral zone—I. Occurrence of emissions during disturbances, *J. Atmos. Terr. Phys.*, 27, 481–497, doi:10.1016/0021-9169(65)90013-9.

Harriman, S. K., E. W. Paschal, and U. S. Inan (2010), Magnetic sensor design for femtotesla low-frequency signals, *IEEE Trans. Geosci. Remote Sens.*, 48, 396–402, doi:10.1109/TGRS.2009.2027694.

Hayakawa, M., Y. Tanaka, and J. Ohtsu (1975), The morphologies of low-latitude and auroral VLF 'hiss', *J. Atmos. Terr. Phys.*, 37, 517–529, doi:10.1016/0021-9169(75)90178-6.

He, M., J. Vogt, H. Lühr, E. Sorbalo, A. Blagau, G. Le, and G. Lu (2012), A high-resolution model of field-aligned currents through empirical orthogonal functions analysis (MFACE), *Geophys. Res. Lett.*, 39, L18105, doi:10.1029/2012GL053168.

Hoffman, R. A., and T. Laaspere (1972), Comparison of very-low-frequency auroral hiss with precipitating low-energy electrons by the use of simultaneous data from two OGO 4 experiments, *J. Geophy. Res.*, 77, 640–650, doi:10.1029/JA077i004p00640.

Hoffman, R. A., R. Fujii, and M. Sugiura (1994), Characteristics of the field-aligned current system in the nighttime sector during auroral substorms, *J. Geophys. Res.*, 99, 21,303–21,325, doi:10.1029/94JA01659.

James, H. G. (1976), Vlf saucers, *J. Geophy. Res.*, 81, 501–514, doi:10.1029/JA081i004p00501.

Jørgensen, T. S (1966), Morphology of VLF hiss zones and their correlation with particle precipitation events, *J. Geophy. Res.*, 71, 1367–1375, doi:10.1029/JZ071i005p01367.

Kamide, Y., and S.-I. Akasofu (1975), The auroral electrojet and global auroral features, *J. Geophy. Res.*, 80, 3585–3602, doi:10.1029/JA080i025p03585.

Laaspere, T., and R. A. Hoffman (1976), New results on the correlation between low-energy electrons and auroral hiss, *J. Geophy. Res.*, 81, 524–530, doi:10.1029/JA081i004p00524.

LaBelle, J., and R. A. Treumann (2002), Auroral radio emissions, 1. Hisses, roars, and bursts, *Space Sci. Rev.*, 101, 295–440.

LaBelle, J., A. T. Weatherwax, M. L. Trimpi, R. Brittain, R. D. Hunsucker, and J. V. Olson (1994), The spectrum of LF/MF/HF radio noise at ground level during substorms, *Geophys. Res. Lett.*, 21, 2749–2752, doi:10.1029/94GL02513.

Lonnqvist, H., M. Andre, L. Matson, A. Bahnsen, L. G. Blomberg, and R. E. Erlandson (1993), Generation of VLF saucer emissions observed by the Viking satellite, *J. Geophys. Res.*, 98, 13,565–13,574, doi:10.1029/93JA00639.

Maggs, J. E. (1976), Coherent generation of VLF hiss, *J. Geophy. Res.*, 81, 1707–1724, doi:10.1029/JA081i010p01707.

Makita, K. (1979), VLF/LF hiss emissions associated with aurora, *Mem. Nat. Ints. Polar Res.*, 16, 1–126.

Mosier, S. R., and D. A. Gurnett (1969), VLF measurements of the Poynting Flux along the geomagnetic field with the Injun 5 satellite, *J. Geophy. Res.*, 74, 5675–5687, doi:10.1029/JA074i024p05675.

Newell, P. T., S. Wing, and C.-I. Meng (2005), Spectral properties and source regions of dayside electron acceleration events, *J. Geophys. Res.*, 110, A11205, doi:10.1029/2005JA011264.

Orlova, K., Y. Shprits, and M. Spasojevic (2016), New global loss model of energetic and relativistic electrons based on Van Allen probes measurements, *J. Geophys. Res. Space Physics*, 121, 1308–1314, doi:10.1002/2015JA021878.

Salvati, M. A., U. S. Inan, T. J. Rosenberg, and A. T. Weatherwax (2000), Solar wind control of polar chorus, *Geophys. Res. Lett.*, 27, 649–652, doi:10.1029/1999GL010702.

Santolík, O., and D. A. Gurnett (2002), Propagation of auroral hiss at high altitudes, *Geophys. Res. Lett.*, 29, 1481, doi:10.1029/2001GL013666.

Sazhin, S. S., K. Bullough, and M. Hayakawa (1993), Auroral hiss—A review, *Planet. Space Sci.*, 41, 153–166, doi:10.1016/0032-0633(93)90045-4.

Sonwalkar, V. S., and J. Harikumar (2000), An explanation of ground observations of auroral hiss: Role of density depletions and meter-scale irregularities, *J. Geophy. Res.*, 105, 18,867–18,883, doi:10.1029/1999JA000302.

Spasojevic, M. (2014), Statistical analysis of ground-based chorus observations during geomagnetic storms, *J. Geophys. Res. Space Physics*, 119, 8299–8317, doi:10.1002/2014JA019975.

Srivastava, R. N. (1976), VLF hiss, visual aurora and the geomagnetic activity, *Planet. Space Sci.*, 24, 375–379, doi:10.1016/0032-0633(76)90050-7.

Torr, M. R., et al. (1995), A far ultraviolet imager for the international solar-terrestrial physics mission, *Space Sci. Rev.*, *71*, 329–383, doi:10.1007/BF00751335.

Tsuruda, K., S. Machida, T. Terasawa, A. Nishida, and K. Maezawa (1982), High spatial attenuation of the Siple transmitter signal and natural VLF chorus observed at ground-based chain stations near Roberval, Quebec, *J. Geophy. Res.*, *87*, 742–750, doi:10.1029/JA087iA02p00742.

Ungstrup, I. M., and D. L. Carpenter (1974), 'Hisslers': Quasi-periodic ($T \sim 2$ s) VLF noise forms at auroral latitudes, *J. Geophy. Res.*, *79*, 5196–5201, doi:10.1029/JA079i034p05196.

Walker, A. D. M. (1974), Excitation of the Earth-ionosphere waveguide by downgoing whistlers. II. Propagation in the magnetic meridian, *Proc. R. Soc. London, Ser. A*, *340*, 375–393, doi:10.1098/rspa.1974.0158.

Xiao, F., Z. Su, H. Zheng, and S. Wang (2009), Modeling of outer radiation belt electrons by multidimensional diffusion process, *J. Geophy. Res.*, *114*, A03201, doi:10.1029/2008JA013580.

Xiao, F., Z. Su, H. Zheng, and S. Wang (2010), Three-dimensional simulations of outer radiation belt electron dynamics including cross-diffusion terms, *J. Geophy. Res.*, *115*, A05216, doi:10.1029/2009JA014541.

Xin, L., D. A. Gurnett, O. Santolík, W. S. Kurth, and G. B. Hospodarsky (2006), Whistler-mode auroral hiss emissions observed near Saturn's B ring, *J. Geophys. Res.*, *111*, A06214, doi:10.1029/2005JA011432.

Yan, X., J. LaBelle, G. Haerendel, M. Spasojevic, N. Bunch, D. I. Golden, H. U. Frey, and A. T. Weatherwax (2013), Dayside auroral hiss observed at South Pole station, *J. Geophys. Res. Space Physics*, *118*, 1220–1230, doi:10.1002/jgra.50141.

Zhelavskaya, I. S., M. Spasojevic, Y. Y. Shprits, and W. S. Kurth (2016), Automated determination of electron density from electric field measurements on the Van Allen Probes spacecraft, *J. Geophys. Res. Space Physics*, *121*, 4611–4625, doi:10.1002/2015JA022132.